Position dependent spatial and spectral resolution measurement of distributed readout superconducting imaging detectors

R. A. Hijmering,[1,a)] P. Verhoeve,[1] A. G. Kozorezov,[2] D. D. E. Martin,[1] J. K. Wigmore,[2] I. Jerjen,[1] R. Venn,[3] and P. J. Groot[4]
[1]*Advanced Studies and Technology Preparation Division, Directorate of Science of the European Space Agency, ESTEC, P.O. Box 299, 2200 AG Noordwijk, The Netherlands*
[2]*Department of Physics, Lancaster University Lancaster LA1 4YB, United Kingdom*
[3]*Cambridge MicroFab Ltd., Broadway, Bourn, Cambridgshire CB3 7TA, United Kingdom*
[4]*Department of Astrophysics, Radboud University Nijmegen, P.O. Box 9010, 6500 GL Nijmegen, The Netherlands*

(Received 15 November 2007; accepted 19 February 2008; published online 29 April 2008)

We present direct measurements of spatial and spectral resolution of cryogenic distributed readout imaging detectors (DROIDs). The spatial and spectral resolutions have been experimentally determined by scanning a 10 μm spot of monochromatic visible light across the detector. The influences of the photon energy, bias voltage, and absorber length and width on the spatial and spectral resolutions have been examined. The confinement of quasiparticles in the readout sensors (superconducting tunnel junctions) as well as the detector's signal amplitude can be optimized by tuning the bias voltage, thereby improving both the spatial and spectral resolutions. Changing the length of the absorber affects the spatial and spectral resolutions in opposite manner, making it an important parameter to optimize the DROID for the application at hand. The results have been used to test expressions for photon energy, position, and spatial and spectral resolutions which have been derived by using an existing one-dimensional model. The model is found to accurately describe the experimental data, but some limitations have been identified. In particular, the model's assumption that the two sensors have identical response characteristics and noise, the approximation of the detailed quasiparticle dynamics in the sensors by border conditions, and the use of a one-dimensional diffusion process is not always adequate. © *2008 American Institute of Physics*. [DOI: 10.1063/1.2907970]

I. INTRODUCTION

Cryogenic detectors are widely used in photon counting spectrophotometers because of their spectroscopic capabilities. A number of systems are currently under development that uses superconductivity as the basis of photon detection. transition edge sensors[1] (TESs) are temperature biased on the superconducting-normal transition and measure the change in temperature due to the absorption of a photon through a change of resistance of the detector. Kinetic inductance detectors[2] (KIDs) rely on the change in inductance caused by the increase in number of quasiparticles (qps) excited by the absorbed photon. When placed inside a resonant circuit, the change in inductance will create a change in resonance frequency of the circuit. A Superconducting Tunnel Junction (STJ) consists of two thin layers of superconducting material separated by an insulating layer. The excited qps tunnel through the insulating barrier to the opposite electrode and, in the presence of a dc bias voltage, produce a measurable current pulse. In each of these detectors, the measurable quantities are proportional to the energy of the absorbed photon, thus providing the intrinsic spectroscopic capability. The best resolutions obtained with cryogenic detectors to date are 0.105 eV at 2.48 eV at optical wavelengths[3] using STJs, while in the x-ray part of the spectrum a resolution of 1.8 eV at 6 keV has recently been achieved by Bandler *et al.* using TESs. While the development of individual devices, up to a few hundreds of microns in size, is well advanced, difficulties arise in the attempt to create larger area detectors which possess equivalent, high spatial, and spectral resolution. The simplest approach is to fabricate close-packed arrays of individual detectors, each with their own signal wire, bias circuit, and readout circuit. This route has been followed in the superconducting tunnel junction camera (S-CAM) project at ESA, in which STJ arrays are being developed as imaging photon detectors for use in optical astronomy. With S-CAM 2 and S-CAM 3 a 6×6 and a 10×12 array of 33×33 μm STJs have successfully been used as optical photon counting spectrometers on the William Hershel telescope (La Palma, Spain) and the Optical Ground Station[5] (Tenerife, Spain). The current camera can handle a count rate up to 8 kHz/pixel and with a maximum resolving power of 14 at 500 nm and microsecond timing accuracy. The thermal load from the signal wires on the cooling system and the size of the readout electronics put a practical limit on the number of pixels which can be read out in this way. A multiplexed readout, in which several pixels share a single signal wire and readout electronics, can considerably extend this limit. In particular, detectors which use superconducting quantum interference device (SQUID)-based readout systems such as TES's are well suited for this. STJs are usually readout with J-FETs at room temperature, which inhibits multiplexed readout, but

a)Electronic mail: rhijmeri@rssd.esa.int.

SQUID readout has also been demonstrated.[6] The readout of KIDs can be conveniently multiplexed by using different resonance frequencies for each KID.

To further increase the sensitive area distributed readout imaging detector (DROID) configurations are being developed. In these devices the photon is absorbed in a single absorbing layer with two or more sensors, in the form of TESs, KIDs, or STJs, at the edges. The resulting excited qps, or phonons in the case of TESs, diffuse rapidly throughout the film and are detected in the sensors. The position of absorption and the energy of the incident photon can be determined from the magnitudes of the sensor responses. Depending on the configuration of the sensor the signal carriers can be free to diffuse in and out of the sensor, be trapped inside the sensor, or some intermediate situation can occur.[7] Trapping of signal carriers inside the sensor will decrease the cross-talk (signal carriers contributing to the signal in both sensors) between the two sensors and increase the signal amplitude of the DROID. This type of trapping should not be confused with local trapping[8] which immobilizes qps either due to the presence of localized states inside the superconductor gap or by localized areas with suppressed gap, e.g., due to impurities, keeping the qps away from the tunnel barrier. Whether or not such a detector is useful in practice depends on whether the spatial and spectral resolutions of the measurements are at least comparable to that of a detector consisting of individual pixels. As will be described below in Sec. II, although there has been great interest in this area, there have been no previous measurements carried out on the dependence of spatial and spectral resolutions of a DROID on the position of the photon absorption.

Although the results shown below are relevant to other types of detectors as well, they are obtained with DROIDs that use STJs as sensors. STJs are sensitive to photon energies ranging from the FIR ($E>2\Delta$) up to the x-ray wavelength range. Due to the low energy gap (typically below 1 meV) the absorption of a photon creates a large number of qps, typically ~2000 for the absorption of an optical photon. The number of qps created is proportional to the incident energy and is given by $N=E_0/\varepsilon$, with N the number of qps, E_0 the energy of the incident photon, and $\varepsilon=1.75\Delta$ the average energy needed to break a Cooper pair. Here Δ is the gap energy and the factor of 1.75 arises from the efficiency of converting the absorbed photon energy into qps.[9] In its lifetime a qp can tunnel many times over the barrier producing an internal amplification.[10] This increases the signal output but adds an extra statistical fluctuation on the charge output. The energy resolution of a STJ is given by $\Delta E(E_0)$ $\delta E(E_0)=2.355[(F+G+J+H)\varepsilon E_0+(K_v+K_H)E_0^2]^{1/2}$, with F the Fano factor, G extra statistical fluctuation due to tunnelling, and J a description of the statistical fluctuations on the converted energy due to loss of productive phonons into the substrate in thin films.[3] The cancelation factor H accounts for the statistical fluctuations in the ratio of direct and cancelation tunnel events.[11] K_v the vertical inhomogeneity factor[3] accounts for the dependence of the deposited energy on the distance between the absorption site and the phonon escape interface between the superconducting material and the substrate, and the horizontal inhomogeneity factor K_H accounts for spatial variations in the responsivity over the area of the device.[12] In addition to these internal noise sources, there are also external sources which influence the resolution such as the electronic noise associated with the readout and possible IR background load. To reduce the current of thermally excited qps, the operating temperature must be well below the critical temperature of the material ($T<0.1T_c$). For the widely used tantalum STJs, with a $\Delta=700$ μeV, the operating temperature lies around 300 mK.

In this paper, we will describe measurements of both spectral and spatial resolutions as a function of absorption position obtained by scanning a monochromatic optical beam with a diameter of 10 μm across the absorber. We used a DROID configuration consisting of an absorber strip of tantalum with a STJ with suppressed gap on each end. The relation between the spectral and spatial resolutions was compared to the result of a one-dimensional (1D) diffusion model of the DROID response by Kraus *et al.*[13] and Jochum *et al.*[14] from which we derived the expressions for the photon energy, absorption position, spectral resolution, and spatial resolution. The measurements were performed as a function of various internal and external parameters to find the optimal conditions for both spectral and spatial resolutions.

II. MODELING OF DROID RESPONSE

Many groups have studied the processes involved with position sensitive detector response and noise factors affecting its resolving power. Kraus *et al.*[13] produced a widely used relation between the spectral and spatial resolutions for DROIDs with perfect qp trapping in the STJs. Jochum *et al.*[14] have produced a generalization of this model in order to include imperfect qp trapping in the STJs. This paper gives the expressions for the charge output for the right (R) and left (L) side STJs in the form

$$Q_{R(+),L(-)}=\frac{E_0 c}{\varepsilon}\frac{\sinh\alpha\left(\frac{1}{2}\pm\frac{x_0}{L}\right)+\beta\cosh\alpha\left(\frac{1}{2}\pm\frac{x_0}{L}\right)}{(1+\beta^2)\sinh\alpha+2\beta\cosh\alpha}. \tag{1}$$

Here $Q_{R,L}$ is a measure for the total number of tunneled electrons collected by the right and left STJs with the "+" sign for the right STJ and the "−" sign for the left STJ, c is the proportionality factor which relates the observed charge to the number of qps reaching the STJ, L is the length of the absorber, and x_0 is the coordinate of the photon absorption position along the 1D DROID. The characteristic parameter describing qp loss inside the absorber $\alpha=L/\sqrt{D\tau_{\mathrm{loss,abs}}}$ is given by the ratio between the length of the absorber and the square root of the product between the diffusion constant D and the loss time in the absorber $\tau_{\mathrm{loss,abs}}$. The parameter β, $\beta=\sqrt{\tau_{\mathrm{tr}}/\tau_{\mathrm{loss,abs}}}$, which is given by the square root of the ratio between the characteristic trapping time τ_{tr} and the loss time in the absorber, has been introduced as a boundary condition to account for partial trapping of qps by the STJ. It describes which fraction of the qps is collected in the STJ and contributes to the measured signal. This is an approximation for the actual in and out fluxes of qps in the STJ because the dynamics of qps in the STJ is more complicated. qps may be

inelastically scattered, the process leading to their trapping, they also may diffuse back into the absorber or they may tunnel, gain energy in the tunnel process and leave the STJ if after the tunnel process, they emerge with sufficiently high energy to diffuse into the absorber. Further processes inside the STJ affecting the charge output as qps loss, trapping by local traps, and multiple tunneling are accounted for by the proportionality factor c.

Segall[11] developed a model for DROIDs with STJs produced from a single superconducting material which included the processes inside the STJs. Later they described the way to control outdiffusion in order to optimize the device.[15] Den Hartog *et al.*[16] produced a two-dimensional (2D) diffusion model without trapping based on the Rothwarf-Taylor equations[17] with which they modeled the current pulse resulting from x-ray absorptions. Ejrnaes *et al.*[18] developed, using a different approach, a similar 2D diffusion model. Adrianov *et al.*[19] have recently developed a 2D diffusion model which takes into account qp loss at the edges of the absorber and qp trapping in the STJs. Also recently Samedov[20] produced a 2D model which gives a relation for the spectral and spatial resolutions, assuming perfect trapping of qp in the STJs. Furlan *et al.*[21] used the model as derived by Jochum *et al.*[14] to analyze the charge output of their devices which they illuminate by using a pulsed light emitting diode to produce single and multiple photon events. To estimate the spectral resolution they used the thermodynamic limit on the resolution.

Based on the original result of Jochum *et al.*,[14] we have now derived all necessary expressions for comparison and interpretation of our experiments. We used an approach similar to that of Kraus *et al.*[13] and found the expressions for the position of the absorption site, photon energy and spectral and spatial resolutions. Specifically we have derived the relation between spatial and spectral resolutions which is useful in the case of uniform illumination when only the spectral resolution can be directly determined. The absorption position depends only on the ratio of the two signals. Thus, rearranging the terms in Eq. (1) and using hyperbolic relations give the following expression for the position as function of the measured charge outputs:

$$x_0 = \frac{L}{2\alpha} \ln\left[\frac{Q_R e^{\alpha/2}(1+\beta) + Q_L e^{-\alpha/2}(1-\beta)}{Q_R e^{-\alpha/2}(1-\beta) + Q_L e^{\alpha/2}(1+\beta)}\right]. \tag{2}$$

Summing the charge outputs in Eq. (1) and rearranging the terms, we obtained the following expression for the energy as function of the measured charge outputs:

$$E_0 = \frac{\varepsilon}{c}\sqrt{(Q_R^2 + Q_L^2)(1-\beta^2) + 2Q_R Q_L[(1+\beta^2)\cosh\alpha + 2\beta\sinh\alpha]} \tag{3}$$

In order to derive spectral and spatial resolution we used the assumption[13] that the uncertainty in the charge measured by either STJ is the same, $\Delta Q_L = \Delta Q_R = \Delta Q$. In general this assumption can not always be justified but it can be justified e.g in the case when electrical noise or when the IR background is the dominant noise contribution. Implicit differentiation with the use of Eqs. (2) and (3) yields the following expressions for spatial and spectral resolutions:

$$\Delta x = \Delta Q \frac{\varepsilon}{E_0 c}\frac{L}{\alpha}\sqrt{[(1+\beta^2)\cosh\alpha + 2\beta\sinh\alpha]\cosh\frac{2x_0\alpha}{L} - (1-\beta^2)}, \tag{4}$$

$$\Delta E = \Delta Q \frac{\varepsilon}{c}\sqrt{[(1+\beta^2)\cosh\alpha + 2\beta\sinh\alpha]\cosh\frac{2x_0\alpha}{L} + (1-\beta^2)}. \tag{5}$$

The relation between the spatial and spectral resolutions becomes

$$\frac{E_0}{\Delta E} = \frac{L}{\Delta x \xi(x_0)}, \tag{6}$$

where $\xi(x_0)$ is given by

$$\xi(x_0) = \alpha\sqrt{\frac{[(1+\beta^2)\cosh\alpha + 2\beta\sinh\alpha]\cosh\frac{2x_0\alpha}{L} + (1-\beta^2)}{[(1+\beta^2)\cosh\alpha + 2\beta\sinh\alpha]\cosh\frac{2x_0\alpha}{L} - (1-\beta^2)}}. \tag{7}$$

When using this model, some limitations need to be kept in mind. Firstly, the model describes a 1D diffusion process. However, for absorptions near the STJ (up to a distance of roughly the width of the absorber away from the STJ), the diffusion process is still 2D. For DROIDs with a smaller aspect ratio this two dimensionality becomes more evident. Secondly, the model assumes the responsivity of the two STJs to be equal. In practice, there are always slight differ-

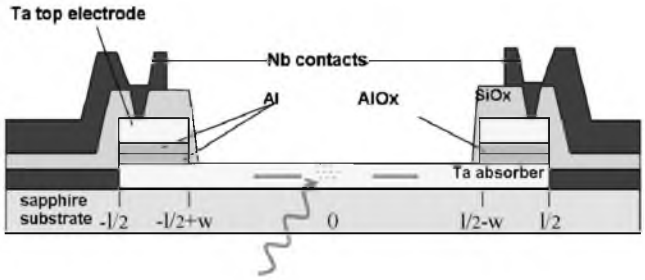

FIG. 1. Schematic representation of the DROID configuration.

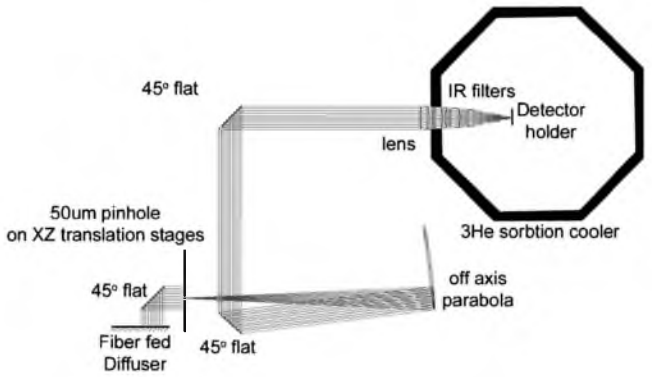

FIG. 2. Schematic representation of the setup.

ences between the STJs due to the fabrication process limitations. This gain difference cannot be corrected for due to the coupling between the two STJs. Thirdly, its validity depends on the assumption of equal noise densities in both STJs. The obvious advantage of the model is that it is simple and treats a general case in which imperfect trapping is taken into account. This situation applies for DROIDs with proximized STJs or KIDS as detectors at the ends of a linear absorber. When taking the limit of $\beta \rightarrow 0$, the case for perfect trapping as given by Kraus *et al.*[13] is retrieved, applicable if, for example, for a DROID with a tantalum absorber and pure aluminium STJs or if TESs are used as detectors.

III. EXPERIMENTAL DETAILS

We have measured the spatial and spectral resolutions as function of photon energy, bias voltage, absorber length (L), and width (w). The experiments were focused around three separate objectives. The first was to experimentally test the theoretical predictions published earlier by Kraus *et al.*[13] and Jochum *et al.*[14] and the resulting derivations in the present paper. Secondly, since the spectral resolution is largely fixed by internal physical processes, we aimed to explore the dependence of the spatial resolution on external variables such as photon energy and bias voltage. Finally, we studied the effect of varying the design of the DROID, notably its length and width.

Several devices of different geometries were produced by Cambridge MicroFab Ltd. (Ref. 22) on a single chip so that variations between devices due to the production process are expected to be small. The devices consist of a 100 nm thick absorber strip of tantalum with a proximized Ta/Al STJ on either end. The STJs have a layout of Ta/Al/AlO_x/Al/Ta with thicknesses of 100/60/1/60/100 nm (Fig. 1). The aluminium layer suppresses the energy gap from 700 to 420 μeV, providing mild trapping to confine the qps in the STJ's area. The tantalum layer of the STJ base electrode is integral with the absorber. The devices have lengths (L_{DROID}) ranging from 200 to 400 μm, all lengths of the DROIDs are including STJs ($L_{\mathrm{DROID}}=L+2w$), and absorber widths of 20, 30, or 50 μm. The STJs are square in geometry with the sides equal to the width of the absorber. The chip is illuminated with optical photons from the back side through the sapphire substrate. The charge output from each STJ is recorded via a pulse height analyzer consisting of a charge sensitive preamplifier followed by a pulse shaping stage, a peak detector, and an analog to digital converter. When signals are detected in the two pulse height analyzers within a time window of 30 μs, the signal is recorded as a single event with the two pulse height amplitudes and the time difference between the two pulses. For responsivity measurements, this method is not ideal because the pulse profile changes with absorption position and the electronics have a fixed integrating time. To first order the effect will show up as an increased loss in the absorber, affecting the value for α. But this should have no significant effect on the resulting spatial and spectral resolution.

The experiments were carried out using a pumped ^{4}He cryostat with a ^{3}He sorption cooler having a base temperature of 295 mK and a hold time of 6.5 h. At this temperature, there is still some thermal current present, acting as an extra noise contribution. On average the subgap current reached a level of 400 pA which is induced by both the thermal current and IR background. The cryostat is fitted with an optical window to allow external illumination with a set of three cold filters placed behind the window to reduce the IR radiation load on the detector. The IR filtering is not 100% efficient and there is still some IR radiation which reaches the detector, degrading the resolutions. However, it justifies the assumption $\Delta Q_L=\Delta Q_R=\Delta Q$, allowing for a simplification to be made in the interpretation of the data. The available wavelength band is 350–750 nm, limited by the IR filters.

The optical arrangement is shown in Fig. 2.[23] The objective was to achieve a spot size of 10 μm. Previous values for spatial resolution of a DROID with 30 nm Al trapping layers estimated from the spectral resolution suggested a spatial resolution of ~40 μm.[24] The spot size of 10 μm should only have a small effect on the measured spatial resolution (3% with a spatial resolution of 40 μm). To produce this spot size on the detector, the high quality optical relay system of the SCAM 3 instrument has been used to image a pinhole on the absorber. A high quality lens was attached to the cryostat to focus the beam on the detector. The rest of the optics consists of two 45° flat mirrors to fold the beam and an off-axis parabola with a 50 μm pinhole in its focus. The pinhole was illuminated using a diffuser which was connected via an optical fiber to a double grating monochromator and a Xe lamp ($\lambda=200-1000$ nm), or, alternatively, to a HeNe laser ($\lambda=633$ nm) for a higher intensity. The pinhole was mounted on a set of translation stages in order to be able to move the spot over the detector chip. The throughput of the complete system was very low necessitating long integrating times due

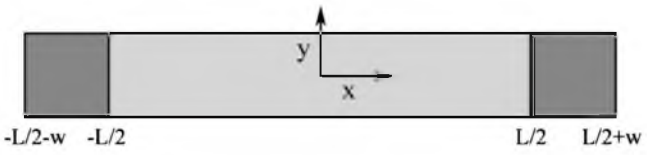

FIG. 3. Schematic representation of the top view of a DROID to indicate the scan directions.

to the low count rate. With the reduction factor of the optical chain of 5.4, this setup should produce a 9.3 μm spot on the detector. The actual size of the light spot has been determined from an intensity profile of a scan over the width of the absorber, in the y direction in Fig. 3.

The resulting intensity profile describes the integration of the image profile with position in one direction. A model of the optical train has shown that the resulting spot profile has a sharp peak with very broad but low intensity wings. This profile has been approximated by a cocentric double 2D Gaussian profile of which the first describes the sharp peak and the second describes the broad wings. The resulting modeled spot profile is integrated in the x direction from $-\infty$ to ∞ (along the length of the absorber). The integration in the y direction between the limits $y'-w/2$ to $y'+w/2$ mimics the movement of the spot across the absorber width.

$$I(y') = \frac{1}{\sqrt{2\pi}} \int_{y'-w/2}^{y'+w/2} \left(\frac{1}{\sqrt{a}} e^{-y^2/2a} + \varphi \frac{1}{\sqrt{b}} e^{-y^2/2b} \right) dy.$$

Here, a is the diameter of the first Gaussian representing the narrow spot and b the diameter of the second Gaussian representing the low intensity broad wings. The intensity of the second Gaussian is given by φ in percentages of the intensity of the first Gaussian. The factor $\sqrt{2\pi}$ results from the integration in the x direction. The measured intensity profile has been normalized to the intensity at the center of the absorber and the model has been fitted to the data, with the result shown in Fig. 4.

The fitted spot profile resulted in a diameter of $a = 10 \pm 1$ μm full width at half maximum (FWHM) for the first, sharp Gaussian and $b = 300 \pm 50$ μm FWHM for the second Gaussian which has an intensity of $\varphi = 0.02 \pm 0.001$. In practice the 10 μm FWHM is shown to be negligible

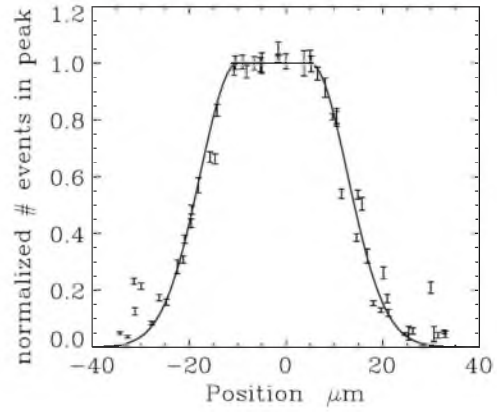

FIG. 4. Measured intensity profile resulting from a scan of the pinhole image over the 30 μm width of the absorber. The solid line is the result of a least-squares fit of the modeled intensity profile to the measured data.

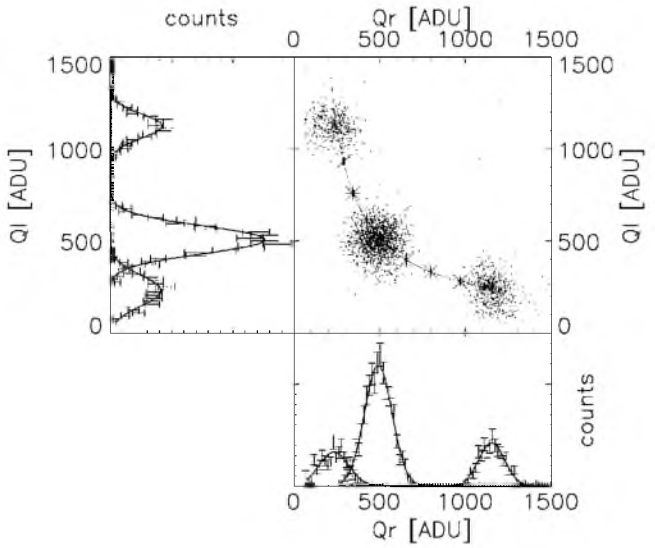

FIG. 5. Scatter plot of three measurements of a single device. The pulse height distributions of the two STJs are plotted on the axis together with the fitted Gaussian profiles. The average charge outputs for the entire scan are shown by stars with the model to obtain the values for α and β as a solid line.

compared to the spatial resolution of the measurements. The 300 μm wide Gaussian will show up as a low intensity background illumination. This spot profile has been used to illuminate the absorber locally on approximately ten positions with different x-coordinates (see Fig. 3) along the absorber, referred to as a "scan". The position of the spot is known from the translation stage settings and verified by detecting the ends of the absorber through a drop in intensity.

IV. RESULTS

The objectives of the experiments are to test the theoretical predictions and to find the optimal configuration of the external and internal parameters. The first of the experiments was carried out on a DROID of length of 400 μm (including STJs) and width of 30 μm with 30×30 μm^2 STJs. Earlier results have shown this geometry to be a good trade off between sensitive area and signal to noise ratio at optical wavelengths.[24] The measurements were carried out by using 410 nm (3.03 eV) photons, determined by optimal throughput of the optical system, with a bias voltage of 120 μV and at a temperature of 295 mK.

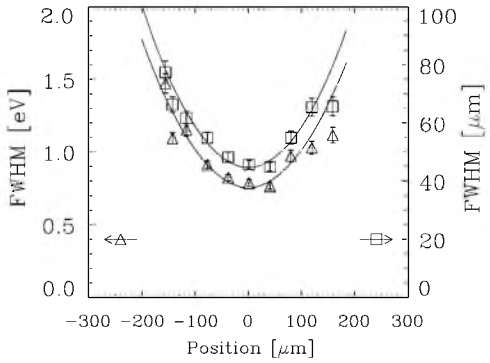

FIG. 6. The measured spectral resolution (triangles) and the measured spatial resolution (squares). The modeled predictions are shown as solid lines.

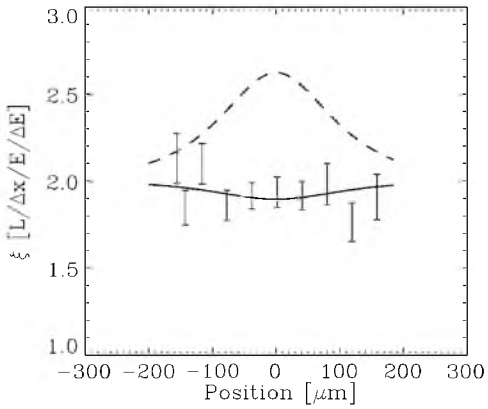

FIG. 7. Relation between the spatial and the spectral resolution with the prediction of the model as a solid line. The dashed line represents the case with perfect trapping (β=0).

Figure 5 shows an example of a scatter plot composed of three measurement points from a single scan. The pulse height distributions are displayed on the sides of the scatter plot. The intensity along the absorber, as indicated by the amplitude of the distribution, varies due to some vignetting in the optical system. A Gaussian profile has been fitted to the pulse height distributions to obtain the charge detected at the left and right STJ. The mean values of the charge obtained for each measurement position in the whole scan are plotted in the Fig. 5 as stars. The values of α and β are determined by obtaining the best fit of Eq. (1) to these charge outputs, also shown in Fig. 5 as a solid line through the measurement points. By using the obtained values for $\alpha = 2.0 \pm 0.1$, $\beta = 1.5 \pm 0.1$, and Eqs. (2) and (3), we calculated the energy and position distributions from the measured data. The values for the mean and FWHM are determined by the Gaussian fit to the spatial and spectral distributions, and the resulting resolutions are shown in Fig. 6, together with the model results.

The spectral and spatial resolutions are best in the center of the absorber (0.77 ± 0.02 eV and 45 ± 2 μm), degrading toward the STJs (1.1 ± 0.04 eV and 65 ± 4 μm). The spectral resolution is relatively poor and limited by electronic noise and the residual IR load on the detector, which causes an effect similar to the electronic noise. Unlike the signal amplitude, the contributions of these noise sources are independent of absorption position, resulting in a strongly position dependent spectral and spatial resolutions. With a spatial resolution of 45 μm, the contribution of the spot size of 10 μm would be $\sim$1 μm and is indeed negligible. The solid lines in Fig. 6 were plotted from Eq. (4) and (5) for best fit values of parameters α and β. For ΔQ in Eqs. (4) and (5), we used an average FWHM of the pulse height distribution of the individual channels over all positions. The variations in the separate measurements are due to the small variations in ΔQ in the different measurements. This variation is strongest near the STJs due to the low count rate caused by vignetting.

TABLE I. Fitting parameters for different photon energy.

E_0 (eV)	α	β	c (ADU/eV)
3.03	2.0 ± 0.1	1.5 ± 0.1	1.3 ± 0.04
2.48	2.1 ± 0.1	1.6 ± 0.1	1.4 ± 0.04
1.97	2.1 ± 0.1	2.0 ± 0.6	1.6 ± 0.2

To test the relation between the spatial and spectral resolutions, the parameter $\xi(x)$ has been evaluated. The experimental values for $\xi(x)$ were determined from the measured spatial and spectral resolutions. The expected values for $\xi(x)$ from the model were calculated by using Eq. (6) and plotted in Fig. 7. The modeled values for $\xi(x)$ agree well with the measurements, showing that the relation between the spatial and spectral resolutions, as given by by Eq. (6), is valid in the case of imperfect trapping. For comparison, $\xi(x)$ for the case of perfect trapping has also been plotted in Fig. 7 (dashed line) to show the potential improvement in spatial resolution for the same spectral resolution.

The 30×400 μm^2 DROID has been scanned with different photon wavelengths; 410, 500, and 633 nm (3.03, 2.48, and 1.97 eV, respectively) which are chosen for optimum throughput of the optical chain. The operating temperature was 295 mK and the STJs were biased at 120 μV. The resulting values of α, β, and the proportionality constant c are shown in Table I. The factor c from Eq. (1) is the proportionality constant between the incident photon energy and the charge output indicating the linearity of the device.

The measured resolving powers ($E_0/\Delta E$ and $L/\Delta x$) for the different photon energies are shown in Fig. 8. Both resolving powers increase with photon energy due to the higher charge output compared to the noise. The resolving powers have been overplotted with the predictions from the model using the values from Table I.

The same DROID has been scanned with 410 nm photons while biased at different voltages (70, 120, and 160 μV) at the operating temperature of 295 mK. Table II shows the

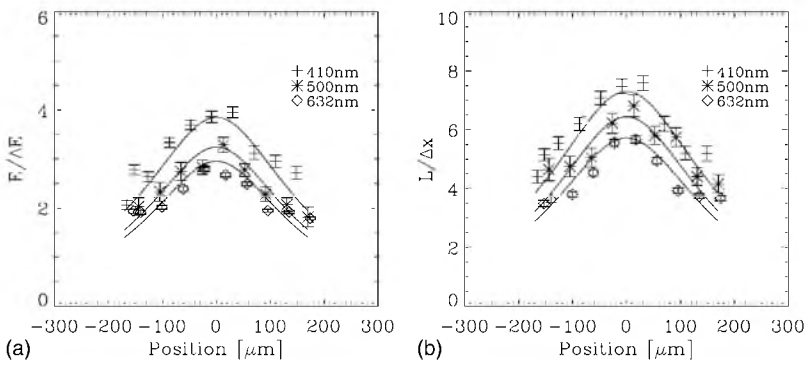

FIG. 8. (a) Spectral resolving power and (b) spatial resolving power vs absorption position for different photon energies. The solid curves show the predictions of the model.

TABLE II. Fitting parameters for different bias voltages.

V_b (μV)	α	β
70	1.9 ± 0.05	0.2 ± 0.05
120	2.0 ± 0.1	1.5 ± 0.1
160	2.0 ± 0.05	2.5 ± 0.1

best fit values for α and β from the different scans. The Ta/Al STJs have a lower energy gap than the pure tantalum absorber, thus producing a mild trapping effect confining qps in the STJs. During the tunnel process, the qps will gain energy by eV_b per tunnel, which is counteracted by relaxation with emission of a phonon. With increasing bias voltage, the probability to reach an energy level above the bulk Ta gap, where the qps can diffuse into the absorber, increases, reducing the trapping effect. This is reflected by the change in the value of β. With decreasing trapping, the probability for cross-talk increases, degrading the spatial resolution.

Figure 9 shows that the effect is most noticeable with a bias voltage of 70 μV. At this bias voltage, a qp needs four tunnels instead of three to reach an energy level above 700 μeV. The spectral resolution is less affected because although the qps escape the STJ they still contribute to the signal in the opposite STJ.

Figure 10 shows the relation $\xi(x)$ for the different bias voltages, and thus different trapping efficiencies, together with the modeled predictions. It is seen that the relation $\xi(x)$ indeed increases with improved trapping going toward the perfect trapping situation shown in Fig. 7.

The spatial and spectral resolutions have been measured for three devices (on the same chip) with different DROID lengths, 200, 300, and 400 μm (30×30 μm^2 STJs included) and a width of 30 μm. The devices have been biased at 120 μV and illuminated with 410 nm photons at an operating temperature of 295 mK. The resulting values for α and β are shown in Table III together with the values for the corresponding characteristic diffusion length $(D\tau_{\mathrm{loss,abs}})^{1/2}$.

The resulting diffusion lengths for the 200 and 400 μm DROIDs are in good agreement, while the 300 μm device shows a slightly larger diffusion length. Comparing the measured resolving powers with the model results, as displayed in Fig. 11, shows that the model does not exactly describe the experiment with the 300 μm DROID. The 200 μm device shows a high value for β. This device shows differences in the responses of both STJs which makes fitting the results

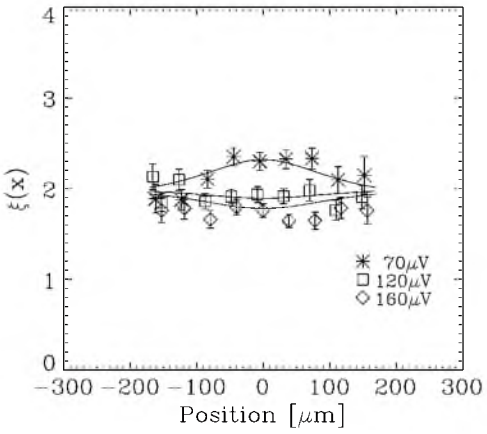

FIG. 10. The ratio between the spatial and spectral resolving powers with position for the different bias voltages with the theoretical prediction of $\xi(x)$ plotted as solid lines.

using a single value for β inadequate. Tests conducted at x-ray energies, where we compared data sets obtained by using the integrating electronics and data sets obtained by using pulse sampling electronics, have shown that the value of β starts to drastically deviate above a value of 2.5 when using the integrating electronics. The true value for β for this measurement is expected to lie between 2.5 and 3.0 instead of at 6.6. This high value may be due to the smallest aspect ratio of this device (see also discussion below).

The spectral and spatial resolving powers for the different absorber lengths are shown in Fig. 11. The spectral resolving power degrades with increasing length while the spatial resolving power improves. This is clearly indicated by the change in the $\xi(x)$ for the different devices, as shown in Fig. 12. The larger losses in longer devices, due to the longer distance to reach the opposite STJ, have the effect of reducing the cross-talk between the STJs. This increases the ratio of the two signals, resulting in improved spatial resolving power. Although the spatial resolving power is increasing with length, the spatial resolution (Δx) remains constant. The average spatial resolution is 45 ± 3 μm at the center of the absorbers for all three lengths. The spectral resolving power decreases with length. This is due to the reduced tunnel probability, and hence lower charge output of the longer devices, for which the STJs are a smaller fraction of entire DROID area. In addition, the electronic noise contribution will remain the same and the IR noise contribution will increase for larger devices.

The chip also contains DROIDs of different absorber

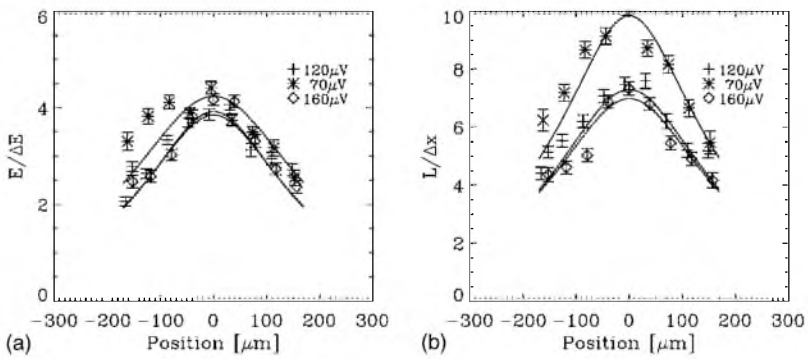

FIG. 9. (a) Spectral resolving power and (b) spatial resolving power vs position at different bias voltages. The solid curves show the predictions of the model.

TABLE III. Fitting parameters for different absorber lengths.

L_{DROID} (μm)	α	β	$(D\tau_{loss,abs})^{1/2}$ (μm)
200	0.8 ± 0.05	6.6 ± 2	175 ± 11
300	1.1 ± 0.05	1.5 ± 0.1	218 ± 10
400	2.0 ± 0.1	1.5 ± 0.1	170 ± 9

widths and hence different STJ sizes. The spectral and spatial resolutions have been measured for three devices with absorber widths of 20, 30, and 50 μm and a total device length L_{DROID}=400 μm. Note that effectively the absorber length L slightly decreases for wider DROIDs with the same length. The DROIDs are biased at 120 μV, illuminated with 410 nm photons at a temperature of 295 mK. The resulting values for α, β, and the diffusion length are listed in Table IV.

The values for α result in an average diffusion length of 185 ± 25 μm, confirming the previously obtained value and the uniformity of the chip. The value of α for the 50 μm device is lower than expected, resulting in a value for the diffusion length outside the error margins of the other devices. The values for β strongly decrease with absorber width. For the larger STJ sizes, the qps spend more time in the STJ leading, to a higher probability of inelastic scattering and trapping. On the other hand, the tunnel probability is increased for larger STJs, which enhances the raising of qp energy and allows easier escape. Clearly, the processes inside the STJs need to be included into the model to exactly understand how STJ size influences the trapping probability.

Figure 13 shows the spectral and spatial resolving powers as a function of absorption position for the three different device widths. The 50 μm wide device clearly shows a discrepancy between the data points and the model. This could be caused by the smaller aspect ratio, making the diffusion process more two-dimensional.

The resulting spectral resolving power shows no obvious difference between the 20 and 30 μm wide devices in Fig. 13. The 50 μm device shows improved resolution which is due to the increased charge output compared to the electronic and IR noise. Although the signal to noise ratio increases, there is no noticeable improvement in the spatial resolution. The improvement in signal to noise with wider devices may be counteracted by the reduced losses due to the slightly shorter absorber length caused by the larger STJ size. Alternatively, if quasiparticle losses at the absorber edges are present in the system, these would be less relevant in wider devices and lead to reduced spatial resolution. For a better understanding of the influence of the absorber width and the presence of edge losses, a more detailed investigation is needed.

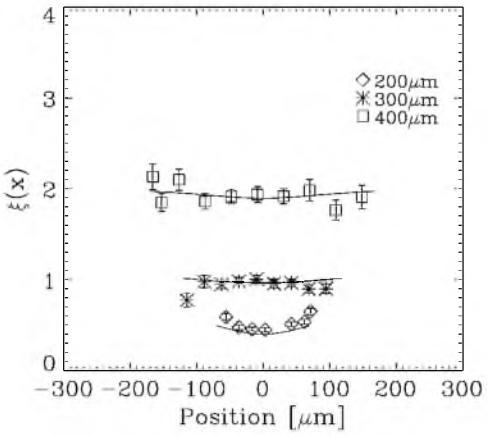

FIG. 12. Relation between the spatial and spectral resolutions for the devices with different absorber lengths. The solid curves show the predictions of the model.

V. DISCUSSION

The experimental results in the previous section clearly show the influence of different parameters on the spatial and spectral resolutions and provide a rigorous test of the simple model. Comparison between the experiment and simulation shows good agreement for both the spectral and spatial resolutions as function of absorption position in Fig. 6, and also for the factor $\xi(x)$ in Fig. 7. The latter is an important result, validating the use of the model to determine the spatial resolution from the measured spectral resolution from a uniform illumination.

The linearity of the energy response of the DROID structure has been tested by using three different photon energies. The factor c in Table I shows the DROID response to be fairly linear with photon energy. The model proved to be consistent in describing the DROID response to variations in photon energy, as shown in Fig. 8. By varying other experimental parameters, such as bias voltage, absorber length, and width, we were able to probe their effect on the detector performance and test the limitations of the model.

The geometry proves to be of great importance for optimization of the DROID performance. The absorber length is the only parameter with which the relation between the spatial and spectral resolutions, as shown by $\xi(x)$ in Fig. 12,

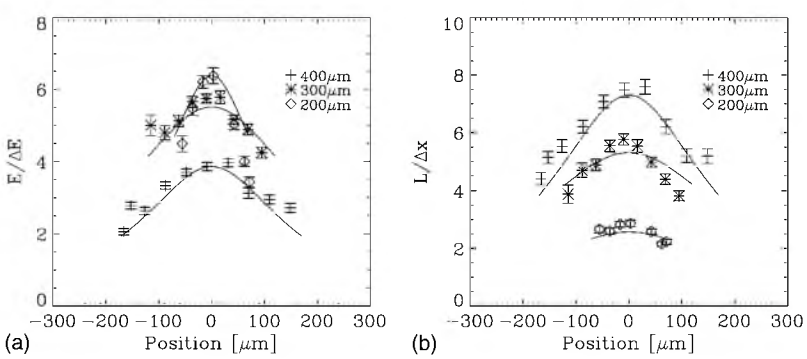

FIG. 11. (a) Spectral resolving power and (b) spatial resolving power vs position for different absorber lengths. The predictions of the model are shown by the solid curves.

TABLE IV. Fitting parameters for different absorber widths.

d (μm)	α	β	$(D\tau_{\mathrm{loss,abs}})^{1/2}$ (μm)
20	2.1 ± 0.05	3.0 ± 0.5	171 ± 4
30	2.0 ± 0.1	1.5 ± 0.1	170 ± 9
50	1.4 ± 0.05	0.6 ± 0.05	214 ± 8

clearly changes. This shows that the length of the absorber is limited by the requirements on the spatial and energy resolutions. The different geometries also provide the clearest evidence on the limitation to the one dimensionality of the model, which is evident in Figs. 11–13 for DROIDs with the smallest aspect ratios. The 1D model cannot account for the dimensionality effects in the results, and for DROIDs with an aspect ratio below 10:1, a 2D model appears to be required. Although these limitations are obvious, nonetheless it is worth mentioning that the basic model is quite robust. The model gives good agreement with the experiments; however, in some cases the fitting parameters α and β will need to go beyond the expected values, as seen with the different geometries. The inability of the model to deal with an asymmetric system is obvious but can easily be dealt with by introducing two separate β-parameters.

Confining the charge carriers inside the sensors is an important mechanism to optimize the spatial and spectral resolutions. With the current DROID configuration, with mild trapping in the STJ, the trapping of qps can be fine tuned with the bias voltage, as shown by Fig. 9. In the model, this process is accounted for by the parameter β which describes the boundary condition just at the infinitesimally thin edge. However, the STJs are extended sensors with their own dynamical properties. The internal processes involving the qps inside the STJ can only be approximately accounted for by a single parameter β, as shown in Tables II and IV. Thus, further development of a DROID model requires modeling of the qp dynamics inside the biased STJ including qp injection, tunneling, and exchange between absorber and STJ. In addition, STJs, and all other sensors, need to be treated as extended objects with appropriate conditions at all their boundaries. The observed dependences on bias voltage and on STJ size are examples since they do not only depend on the imperfect trapping but also on the combination of other parameters of the STJ. For physical reasons, this dependence can be understood but cannot be predicted by using the current simple model. Nonetheless, the simple model is invaluable in setting up a basic framework for DROID optimization.

The final limitation of the model is the assumption $\Delta Q_R=\Delta Q_L$, independent of position. In our experiments this limitation has been obscured by the presence of IR background and electronic noise. Their contributions dominate the measured resolutions and they are independent of signal amplitude, ensuring that the assumption above is validated (as long as the STJs are identical). However, they induce a strong position dependency of the spectral and spatial resolutions (cf. Fig. 6), which is an unwanted property for a practical detector. The full scale problem of obtaining the best resolutions will become evident if the contribution of these external noise sources is reduced in an optimized experimental configuration, and the intrinsic noise sources (which scale with signal amplitude) become dominant. This, is expected to reduce the position dependency of the resolutions. Then, any further development on an improved model must rest on breaking down all contributing noise factors. For DROIDs with STJs as sensors such a breakdown will be in a similar form as with single STJs, as shown in the Introduction. All noise factors which are important for single STJs will of course play an important role when it becomes part of a DROID. However, additional noise sources will appear, some of which will be dependent on absorption position.

VI. CONCLUSION

In summary, we have developed an experimental technique to measure the spectral and spatial resolutions in distributed readout imaging devices directly for each photon absorption position. By using this technique, we have explored the influence of several parameters on the spatial and spectral resolutions. By using the model of Jochem *et al.*, we have derived the expressions for photon energy, photon absorption position, and the resolutions which give a satisfactory description of the experimental data. The limitations of the model where tested experimentally and major restrictions were identified, pointing out the necessity for further development of the theoretical model along the described directions.

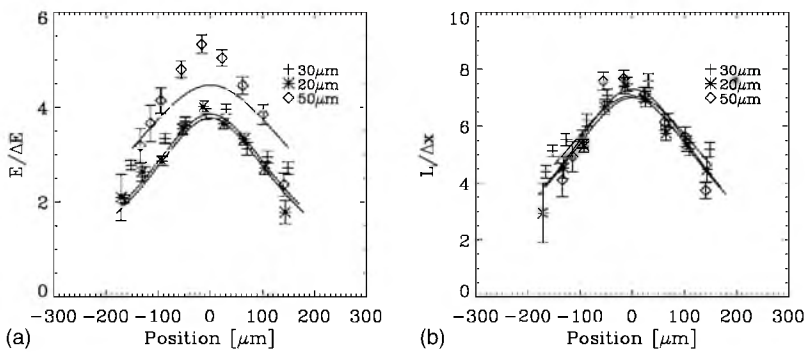

FIG. 13. (a) Spectral resolving power and (b) spatial resolving power vs position for different absorber widths. The solid curves show the predictions of the model.

[1]K. D. Irwin, Appl. Phys. Lett. **66**, 1998 (1995).
[2]P. Day, H. Leduc, B. Mazin, A. Vayonakis, and J. Zmuidzinas, Nature (London) **425**, 817 (2003).
[3]D. D. E. Martin, P. Verhoeve, A. Peacock, A. G. Kozorezov, J. K. Wigmore, H. Rogalla, and R. Venn, Appl. Phys. Lett. **88**, 123510 (2006).
[4]S. Bandler, R. Brekosky, A. Brown, J. Chervenak, E. Figueroa-Feliciano, F. Finkbeiner, N. Iyomoto, R. Kelly, C. Kilbourne, F. Porter, J. Sadleir, and S. Smith, Low Temp. Phys., **151**, 400 (2008).
[5]D. D. E. Martin, P. Verhoeve, T. Oosterbroek, R. A. Hijmering, T. Peacock, and R. Schulz, Proc. SPIE **2006**, 6269.
[6]C. A. Mears, S. E. Labov, M. Frank, H. Netel, L. J. Hiller, M. A. Lindeman, D. Chow, and A. T. Barfknecht, IEEE Trans. Appl. Supercond. **7**, 3415 (1997).
[7]N. E. Booth, Appl. Phys. Lett. **50**, 293 (1987).
[8]A. G. Kozorezov, R. A. Hijmering, G. Brammertz, J. K. Wigmore, A. Peacock, D. Martin, P. Verhoeve, A. A. Golubov, and H. Rogalla, Phys. Rev. B **77**, 014501 (2008).
[9]M. Kurakado, Nucl. Instrum. Methods Phys. Res. **196**, 275 (1982).
[10]K. E. Gray, Appl. Phys. Lett. **32**, 39 (1978).
[11]K. Segal, Ph.D. thesis, Yale University, 2000.
[12]P. Verhoeve, N. Rando, J. Verveer, A. Peacock, A. van Dordrecht, P. Videler, M. Bavdaz, D. J. Goldie, T. Lederer, F. Scholze, G. Ulm, and R. Venn, Phys. Rev. B **53**, 809 (1996).
[13]H. Kraus, F. V. Feilitzsch, J. Jochum, R. L. Mössbauer, Th. Peterreins, and F. Probst, Phys. Lett. B **231**, 2 (1989).
[14]J. Jochum, H. Kraus, M. Gutsche, B. Kemmather, F. V. Feillitzsch, and R. L. Mössbauer, Ann. Phys. **2**(7), 611-634 (1993).
[15]V. Savu, L. Li, A. Mukherjee, C. M. Wilson, L. Frunzio, D. E. Prober, and R. J. Schoelkopf, Nucl. Instrum. Methods Phys. Res. B **520**, 237 (2004).
[16]R. den Hartog, D. Martin, A. Kozorezov, P. Verhoeve, N. Rando, A. Peacock, G. Brammetrz, M. Krumrey, D. J. Goldie, and R. Venn, Proc. SPIE **2000**, 4012.
[17]A. Rothwarf and B. N. Taylor, Phys. Rev. Lett. **19**, 27 (1967).
[18]M. Ejrnaes, C. Nappi, and R. Cristiano, IEEE Photonics Technol. Lett. **18**, 953 (2005).
[19]V. Adrianov, L. Filippenko, V. P. Gorkov, and V. Koshelets, Low Temp. Phys. **151**, 287 (2008).
[20]V. Samedov, Low Temp. Phys. **151**, 333 (2008).
[21]M. Furlan, E. Kirk, and A. Zehnder, J. Appl. Phys. **101**, 054501 (2007).
[22]G. Brammertz, Ph.D. thesis, University of Twente, 2003.
[23]R. A. Hijmering, P. Verhoeve, D. D. E. Martin, I. Jerjen, A. G. Kozorezov, and R. Venn, Low Temp. Phys. **151**, 298 (2008).
[24]R. A. Hijmering, P. Verhoeve, D. D. E. Martin, A. Peacock, A. G. Kozorezov, and R. Venn, Nucl. Instrum. Methods Phys. Res. A **559** 692 (2006).